

Predictable thermoelectric performance of directly synthesized Bi_{0.5}Sb_{1.5}Te₃ using laser powder bed fusion additive manufacturing

Jianxu Shi ^{a,b,1}, Zhiqiang Tong ^{b,1}, Chunjiang Wang ^b, Bobo Li ^{c,d}, Shengli Cao ^a, Yihui Hu ^a, Zhicang Wang ^a, Jun Peng ^{c,*}

^a School of Automation, Xi'an University of Posts and Telecommunications, Xi'an, Shaanxi, 710121, China

^b State Key Laboratory for Manufacturing Systems Engineering, Xi'an Jiaotong University, Xi'an, Shaanxi, 710049, China

^c School of Mechanical Engineering, Xi'an Jiaotong University, Xi'an, Shaanxi, 710049, China

^d National Innovation Institute of Additive Manufacturing, No. 997, Shanglinyuan 8th Road, Gaoxin District, Xi'an 710300, China



ARTICLE INFO

Handling Editor: Dr P. Vincenzini

Keywords:

Thermoelectric materials
Ternary Bi_{0.5}Sb_{1.5}Te₃
Laser powder bed fusion
Direct synthesis
Flexible devices

ABSTRACT

Laser powder bed fusion (LPBF) additive manufacturing, as a novel technique provides broad benefits in thermoelectric materials synthesis, such as enhanced printing speed, reduced waste materials, and customized dimension design. The high energy density of laser could potentially balance the synthesis rate and thermoelectric figure-of-merit zT , but the correlations between laser energy and material performance are still vague. Herein, Bi_{0.5}Sb_{1.5}Te₃ bulks are directly synthesized by LPBF with a recorded synthesis rate of 254 g h⁻¹. The maximum zT , without any post-processing, reaches 1.1 at 75 °C. Induced nanoscale pores by high laser energy printing, obtain a comparable diameter to phonon mean free path, leading to reduced lattice thermal conductivity and enhanced TE performance. We found that input laser energy critically affected thermoelectric performance and concluded the correlation between volumetric energy density E_V and power factor PF , $PF = 9.05E_V^2 - 30.01E_V + 48.84$. It potentially predicts thermoelectric performance with inputted laser energy density.

1. Introduction

Harvesting heat energy is a novel emerging technique as a distributive power source that can comprehensively scavenge thermal gradient from the human skin surface, solar heat, and industrial waste heat [1]. The energy conversion process is triggered by an applied temperature gradient in which charge carriers of thermoelectric (TE) material diffuse and accumulate on the cold side. This is the Seebeck effect to generate electric voltage potential converted from the temperature difference. Conversely, the Peltier effect is used to create temperature differences with an applied voltage [2–5]. To evaluate the TE materials properties, the dimensionless figure-of-merit ($zT = S^2\sigma T/k$) has been defined, where S , σ , T , and k denote Seebeck coefficient, electrical conductivity, absolute temperature, and total thermal conductivity, respectively [6–12]. These intrinsic material parameters have opposite dependence on carrier densities [13]. Therefore, an ideal TE material simultaneously requires a high power factor PF ($PF = S^2\sigma$), together with low total thermal conductivity. Recently, various high-performance TE materials and devices are emerging, such as promising candidates SnSe [14], Ag₂Se [15],

Mg₃(Bi, Sb)₂ [16], TlCu₃Te₂ [17,18], ionic TE materials [19], and prospective wearable TE device [20,21].

Among many reported TE materials, bismuth telluride (Bi₂Te₃) based alloys are still commercially available for applications around ambient temperature. Although TE materials and devices indicate extensive potential, successful applications are still limited, partially because of time-consuming conventional fabrication processes, like ball-mill alloying, hot-press sintering, and spark plasma sintering [22]. These bath syntheses restrict modules and configurations design and require post-processing to form expected configurations.

Laser powder bed fusion (LPBF) additive manufacturing, fortunately, helps to directly synthesize TE materials and fabricate structured modules in one step. Laser is an effective energy source to melt raw powders and so it is broadly used in 3D printing techniques. According to the differences in powder melting and feeding system, it involves selective laser melting (SLM)/LPBF [23,24], selective laser sintering (SLS) [25–27], multi-coaxial powder feed laser engineering net-shaping (LENS) [28]. Nowadays, the LPBF technique is widely reported to 3d-print Ti6Al4V [29], high-entropy alloys [30], NiTi alloys [31], and

* Corresponding author.

E-mail address: pengjun@xjtu.edu.cn (J. Peng).

¹ These authors contributed equally to this work.

W–Cu multi-material [32].

Recently, LPBF has been applied to fabricate TE materials. Printed TE materials can be classified into two categories: (1) TE alloy powders or (2) TE individual elemental powders are adopted for printing original materials. For the former, LeBlanc et al. (2016) reported initial research on the melt line evolution of Bi₂Te₃ by the LPBF process and demonstrated its printability [33]. They followed (2017) presented and printed Bi₂Te₃ with columnar microstructure to enhance electrical properties [34,35], but also cause reduced electrical conductivity [36]. Yan et al. (2017) reported LPBF-based *n*-type Bi₂Te_{2.7}Se_{0.3} workpieces and found secondary phases which decreased figure-of-merit [37]. In 2019, Bi_{0.4}Sb_{1.6}Te₃ alloy powders were successfully printed into bulks with oriented crystals by LPBF, but materials indicated relatively low *zT* 0.7 and 0.2 along different building directions [38]. Zhang et al. (2022) proposed volumetric energy density as a useful guide, while no further report on *zT* [39]. For the latter, In 2021, our previous work reported that Sb₂Te₃ binary system was synthesized by LPBF printing individual elemental powders, and the parts had *zT* 0.4 [40]. Yang et al. (2022) successfully synthesized highly oriented BiTeSe by LPBF from elemental materials of Bi, Te, and Se powders. However, the thickness of the printed sample was too thin to measure TE properties along the building direction [41]. Beyond bismuth telluride, some other TE materials also can be synthesized by LPBF. For instance, Mn–Si alloys [42], SnTe [43,44], CoSb_{2.85}Te_{0.15} skutterudite [45], half-heusler [46,47], Mn–Al–Si alloys, and SrTiO₃ were synthesized by Kinemuchi et al. (2016) [48]. More detailed and comprehensive research works about additive manufacturing of TE bulk in review publications were summarized by the LeBlanc group [49]. However, it has not been reported yet regarding high-performance *p*-type BiSbTe TE materials using the LPBF method from the pseudo-homogeneous mixture of elemental powders.

In this work, the LPBF technique was used to directly synthesize dense *p*-type Bi_{0.5}Sb_{1.5}Te₃ (BiSbTe) polycrystalline TE materials on a large scale (about 600 g in a batch). According to Bi_{0.5}Sb_{1.5}Te₃ stoichiometric ratio, the well-mixed raw Bi, Sb, and Te elemental powders were ball-milled with excess Te powder. The phases, microstructure, and anisotropic thermoelectric performance of LPBF-printed BiSbTe bulks were systematically studied to quantify the manufacturing dependence of thermoelectric performance. The correlation between thermoelectric power factor *PF* and volumetric energy density of laser *E_V* was found, *PF* = 9.05*E_V*² – 30.01*E_V* + 48.84. When *E_V* increased from 1.5 to 2.4 J mm⁻³, the corresponding peak *PF* increased from 11.9 to 31.4 μW cm⁻¹ K⁻². Layer-by-layer printing orders also affected thermoelectric performance, leading to anisotropic *zT* values. The maximum *zT* of 1.1 at 75 °C along a building direction was obtained, and it was approximately triple times higher than that of counterparts along the perpendicular direction. Additionally, a unidirectional flexible TE device using directly LPBF printed *p*-type legs were demonstrated and exhibited stable power output performance. The clarified manufacturing dependence can not only helpfully enhance the performance of thermoelectric materials, but also prove LPBF approach could enlarge the scope of device structure design through one-step direct synthesis.

2. Methods

2.1. Synthesis

Highly purified raw elements of Bi, Sb, and Te powders (all, 99.99% under 100 mesh, CNBM Optoelectronic Materials Co., Ltd, Chengdu, China) were accurately weighed according to the Bi_{0.5}Sb_{1.5}Te₃ stoichiometric ratio with excess 5 wt% Te powders. Subsequently, 600 g of powder was evenly mixed using a planetary ball milling at 160 rpm for 5 h. The forward and reverse ball milling time was half an hour, and the pause time was 1 min. The weight ratio of the milling balls to starting powder was 1:46. The zirconia mill-ball were two 10 mm and one 15.5 mm in diameter. These process parameters have also been used to mix antimony and tellurium powders [40]. The mixture was spread on a

stainless-steel substrate into a powder bed with a 2 mm thickness in a homemade laser 3D printer. The processing parameters of LPBF processed mixture powders are shown in Table S1, and the orthogonal scanning strategy was selected as the scan mode. Laser melting twice for every alloyed layer was used to fully react and form densified thermoelectric bulk. The sample number was marked as S number - laser volumetric energy density, for example, S1-1.5. A commercial laser was used for the synthetic LPBF process. The maximum output power, wavelength, and spot diameter of the laser were 500 W, 1070 nm, and 100 μm, respectively. Alloying by LPBF process was carried out under high-purity argon (1.5–2.0 kPa). Additionally, a synchronous thermal analyzer (Metter Toledo TGA/DSC3+) was used to simulate the alloying process of alloying for the Bi, Sb, and Te powder during additive manufacturing.

2.2. Characterization

The morphology of the microstructure of printed samples, which were ground with sandpaper in different mesh of 400, 800, 1000 and 1200 respectively, and then polished with 1 μm diamond suspension, was investigated using scanning electron microscopy (SEM, TESCAN MAIA3 LMH) with energy-dispersive X-ray spectroscope (EDS). The phase composition and crystal structure of laser additive-manufactured samples were examined by an XRD analyzer (Bruker, D8) with a Cu- $\text{K}\alpha$ radiation (wavelength of 0.15418 nm) at room temperature, using the scanning step of 0.02°, range from 10° to 80°. The X-ray source was operated at 40 kV and 40 mA. The size distribution of well-mixed powder and particle sizes were approximately less than 50 μm shown in Fig. S1. Fig. S2 a, b, c, d, and e noted the uniformity and morphology of elemental mixed powders. Fig. S2 f presented the XRD pattern of three elemental mixtures composed of the superposition of three elemental elements patterns, indicating that no extra alloying was produced during ball milling. The crystal orientation was analyzed by electron back-scatter diffraction (EBSD, Oxford Nordlys-CMOS detector). The accelerating voltage, sample slope, acquisition speed, and step size in EBSD were 15 KV, 70°, 99.35Hz, and 1 μm, respectively. The EBSD sample, excepting mechanical polishing, was polished on multifunctional ion thinner (Leica EM RES102), at 5 kV with an inclination of 10° for 30 min, to eliminate the stressed layer. Transmission electron microscopy (TEM, JEOL JEM-F200) with EDS was used to observe and analyze the synthetic uniformity of printed samples at the nanoscale, with an acceleration voltage of 200 kV. The preparation of TEM samples was ultrasonically peeled from printed Bi_{0.5}Sb_{1.5}Te₃ (BST) ingots. The BST powder with a particle size of 100 μm was obtained from manual grinding printed ingot. The 1 g BST powder was put into a 50 ml centrifuge tube with alcohol. The ultrasonic power, temperature, and time were 100 W, 40 °C, and 30 h, respectively. The sample was placed in a high-speed centrifuge (TG16G, Henan Yaogong Instrument Equipment Co., Ltd, Zhengzhou, China), at a speed of 10000 rpm for 10 min. After centrifugation, 10 ml supernatant was taken into a 50 ml centrifuge tube with alcohol. The second ultrasonic power, temperature, and time were 100 W, 40 °C, and 20 h, respectively. The sonicated solution was dropped on the copper grid with carbon film, evaporating alcohol at room temperature for 30 min, to prepare the TEM sample.

The electrical transport properties (Seebeck coefficient *S* and electrical conductivity σ) were measured by ULVAC ZEM-3 at the temperature range of 25 °C–250 °C in a helium atmosphere. The bar-shaped sample size had approximate dimensions of 3 mm × 3 mm × 10 mm. The thermal conductivity *k* was given from the relationship *k*=*D*C_P*d*, where *D* is the thermal diffusivity. Square with dimensions 6 mm × 6 mm × 2 mm were utilized for thermal diffusivity measurement by a laser flash method (Netzsch, LFA467, Germany). C_P is the specific heat obtained by the Dulong-Petit law. The *d* is density measured by the Archimedes method. According to the measurements, the uncertainty of the Seebeck coefficient, electrical conductivity, and thermal conductivity were less than 5 %, 2 %, and 5 %, respectively. The Hall coefficient

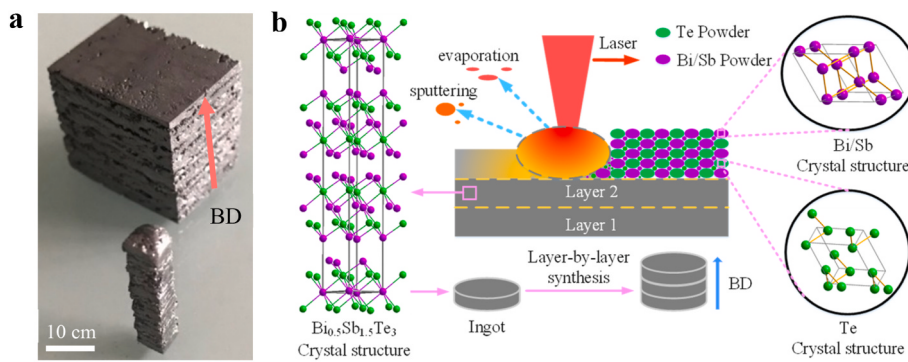


Fig. 1. **a**, $\text{Bi}_{0.5}\text{Sb}_{1.5}\text{Te}_3$ bulks were directly printed along the building direction (BD). **b**, Schematic diagram indicated the process of laser powder bed fusion (LPBF) additive manufacturing. $\text{Bi}_{0.5}\text{Sb}_{1.5}\text{Te}_3$ TE materials were layer-by-layer synthesized from individual elemental powders.

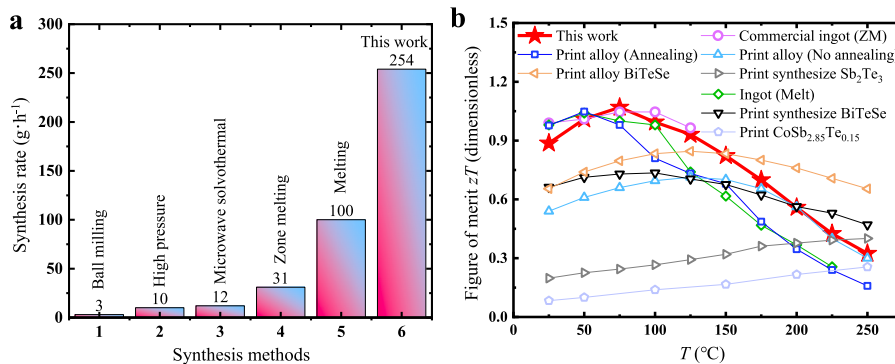


Fig. 2. **a**, The synthesis rate by LPBF in this work accomplished the highest record in comparison with that of other regular techniques. **b**, The maximum zT of synthesized samples by LPBF is 1.1 at 75 °C which is higher than that of LPBF-based bismuth telluride family and some regular TE materials.

at room temperature was verified using a Hall measurement system (HET-RT, JouleYacht, China), with a magnetic field of 0.6 T. The corresponding carrier concentration n and carrier mobility μ were calculated due to the equations $n = 1/(eR_H)$ and $\mu = \sigma R_H$, respectively, where e denoted electron charge.

3. Results and discussion

Laser powder bed fusion (LPBF) additive manufacturing illustrated the potential to directly synthesize thermoelectric materials or devices with designed configurations. Layer-structured $\text{Bi}_{0.5}\text{Sb}_{1.5}\text{Te}_3$ bulks were efficiently printed from elemental powders, indicating the printability of specified geometry and structures. Prismatic and cubic samples were prepared for measurements shown in Fig. 1 a. Laser energy is the main power to continuously melt Be/Sb and Te powder mixtures, and synthesize $\text{Bi}_{0.5}\text{Sb}_{1.5}\text{Te}_3$ multilayers. A schematic diagram describes the process of LPBF additive manufacturing and crystal structures (Fig. 1 b). The high energy density of the laser can not only help to achieve the specific crystal structure of quintuple layers of $\text{Bi}_{0.5}\text{Sb}_{1.5}\text{Te}_3$ to improve thermoelectric performance, but also enhance the processing rate. The LPBF manufacturing in this work indicated the highest record of synthesis rate, 254 g per hour, compared with that of other techniques, such as zone melting, microwave solvothermal, high pressure, and ball milling (Fig. 2 a). The calculations of the synthesis rate are listed in Table S2. The peak zT of LPBF synthesized $\text{Bi}_{0.5}\text{Sb}_{1.5}\text{Te}_3$ samples is competitive to printed bismuth telluride family and classic TE materials by other techniques [38,40,41,45,50–52], as shown in Fig. 2 b. To understand intensified thermoelectric performance, compositions, and microstructures were deeply characterized.

Materials properties and thermoelectric performance of LPBF-ed bulks were critically affected by microstructure in micro- and nano-

scales. The SEM image of LPBF-ed bulks showed no obvious impurities, which confirmed the effectiveness of the LPBF preparation process in Fig. 3 a. Energy dispersive X-ray spectroscopy (EDS) mapping in Fig. 3 b exhibited uniform distribution of Bi, Se, and Te elements at the micron scale. The composition analysis from EDS were shown in Table S3. While some tested compositions had a little difference from target values, it was still acceptable. The electron backscatter diffraction (EBSD) in Fig. 3 c suggested widely distributed grain size with obvious crystallographic orientations preferentially along the laser moving direction. The textured microstructure was beneficial to the enhancement of thermoelectric performance by increasing charge carrier transports and confining lattice thermal vibrations, leading to enhanced zT [38,53]. To further investigate uniformity and microstructures in a nano-scale, the EDS mapping and corresponding electron image in Fig. 3 d₁-d₄ showed that the preparation process could achieve uniform elemental distributions at the nanoscale. The morphology and structural features at the nanoscale were characterized by the TEM, and corresponding selected area electron diffraction (SAED) patterns of polycrystalline structure in the inset (Fig. 3 e). The HRTEM pictures of the LPBF-ed $\text{Bi}_{0.5}\text{Sb}_{1.5}\text{Te}_3$ sample were characterized in Fig. 3 f, and the fringe width (0.32 nm) displayed in the inset was in a good agreement with the standard interplanar spacing of the $\text{Bi}_{0.5}\text{Sb}_{1.5}\text{Te}_3$ crystal structure ($d_{(015)} = 0.317$ nm). The preferred growth orientation was also clearly observed and highlighted in the inset. The HRTEM characterization confirms lattice distortions induced by the complex thermal history of the LPBF 3D printing process. The lattice distortions presumably help to reinforce phonon scattering. The comparable structures and effects of lattice distortions were also reported in the study of the microstructural evolution of 304 L stainless steel fabricated by LPBF [54].

In addition, the phase change in the LPBF process was also studied by thermogravimetric analysis (TGA)-differential scanning calorimeter

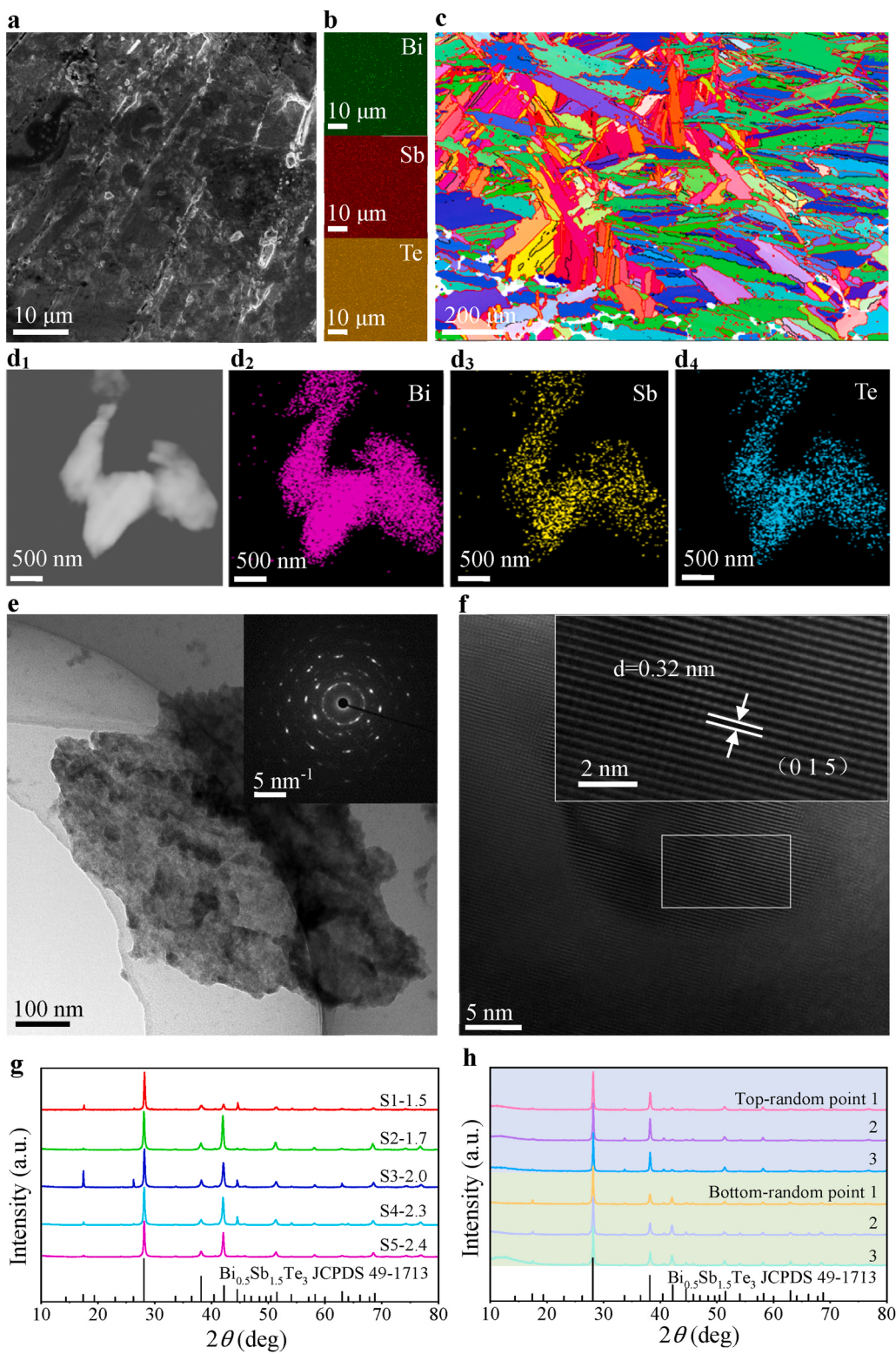


Fig. 3. **a**, SEM images of layer-by-layer microstructures. **b**, Energy dispersive X-ray spectroscopy (EDS) mapping of uniformly distributed Bi, Se, and Te elements. **c**, Electron backscatter diffraction (EBSD) indicated widely distributed grain size with obvious crystallographic orientations along the laser moving direction. **d₁-d₄**, Electron images and EDS mapping in the nanoscale. **e**, TEM, and corresponding selected area electron-diffraction pattern in the inset. **f**, HRTEM images described the similarity in fringe width with the standard interplanar spacing. **g**, XRD pattern of various samples with different laser energetic densities. **h**, Identified powder diffraction peaks on six randomly selected surface points of the sample S5-2.4.

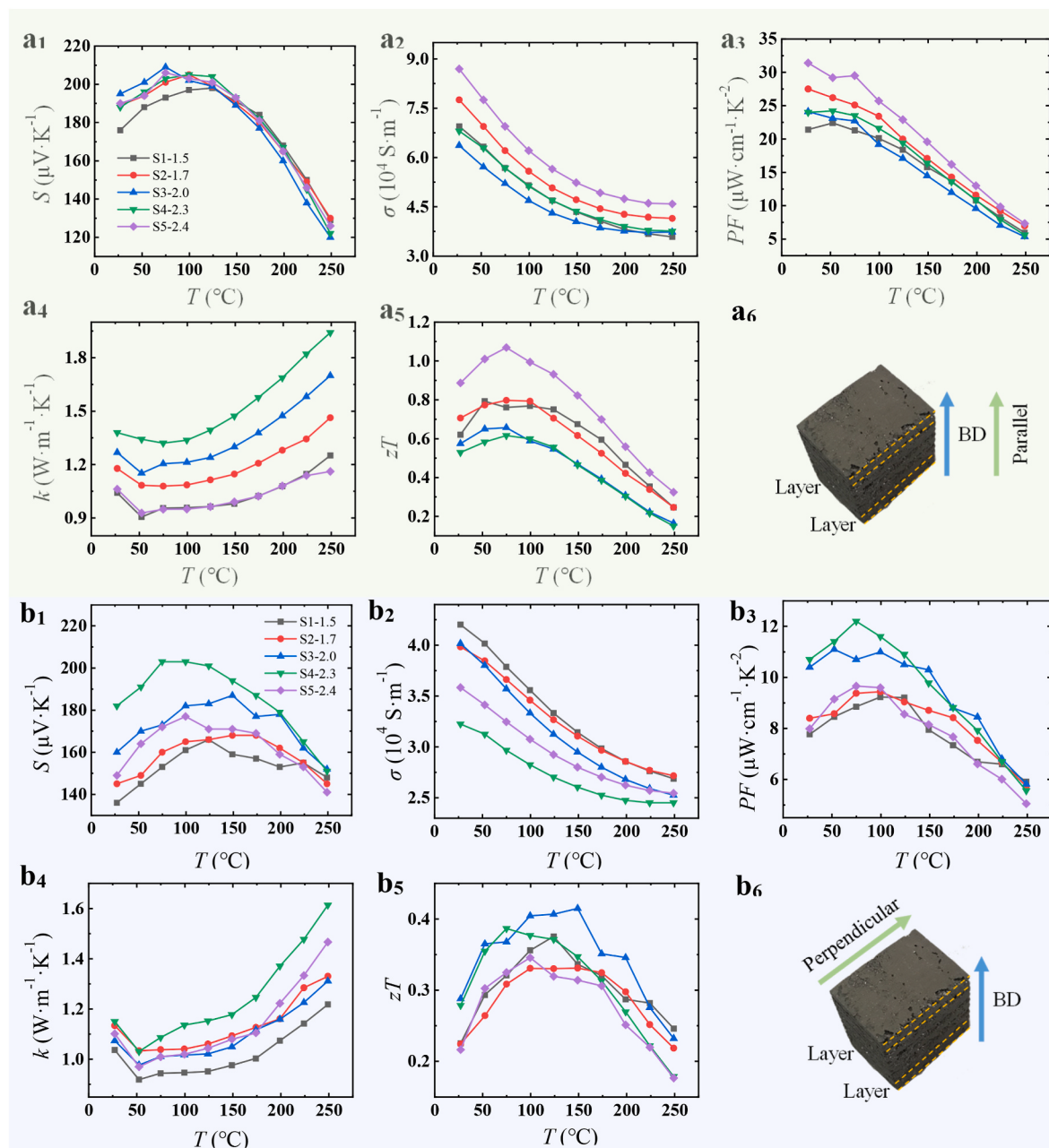


Fig. 4. TE performance of the printed $\text{Bi}_{0.5}\text{Sb}_{1.5}\text{Te}_3$ bulks along parallel and perpendicular directions, respectively to the building direction (BD). **a₁** and **b₁**, Seebeck coefficient. **a₂** and **b₂**, Electrical conductivity. **a₃** and **b₃**, Power factor. **a₄** and **b₄**, Total thermal conductivity. **a₅** and **b₅**, Figure-of-merit zT . **a₆** and **b₆**, Photographs of printed sample in parallel and perpendicular directions.

(DSC), and detailed analysis was shown in Supplementary Information (Fig. S3 and Fig. S4). The powder diffraction peaks could be indexed to the standard pattern of $\text{Bi}_{0.5}\text{Sb}_{1.5}\text{Te}_3$, as shown in Fig. 3 g, implying that no other secondary phases were produced. To further characterize the uniformity of the additive-manufacturing thermoelectric materials, six randomly selected points on the top and bottom surfaces of sample S5-2.4 were scanned, and the powder diffraction peaks were consistently identified according to the standard pattern JCPDS 49–1713, as shown in Fig. 3 h.

Temperature dependences and anisotropies of Seebeck coefficient (S), electrical conductivity (σ), power factor (PF), total thermal conductivity (k), and figure-of-merit (zT) along various directions were investigated and plotted in Fig. 4. The Seebeck coefficient of various bulks presented similar change trend from ambient temperature up to 250 °C. The corresponding temperature of the peak Seebeck coefficient

approached to lower temperatures with the increase of laser energy density. Note that the Seebeck coefficient, the electrical conductivity, and the calculated power factor were improved with higher laser energy density. The electrical transport property was increased from $11.9 \mu\text{W cm}^{-1} \text{K}^{-2}$ (1.6 J mm^{-3}) to $31.4 \mu\text{W cm}^{-1} \text{K}^{-2}$ (2.4 J mm^{-3}) at room temperature, while the total thermal conductivity had no similar trend due to the reduced density of sample S5-2.4 as a transition point. The vaporization of Te powder could occur at a high laser energy level because the heat of vaporization of the element tellurium 114 kJ mol^{-1} was much lower than that of the element bismuth 179 kJ mol^{-1} and antimony 193 kJ mol^{-1} .

It could be seen from Fig. 4 a₁-a₅ and Fig. 4 b₁-b₅ that the thermo-electric properties exhibited strong anisotropy along parallel and perpendicular directions respectively to the building direction (BD, highlighted). The Seebeck coefficient of all samples along the parallel

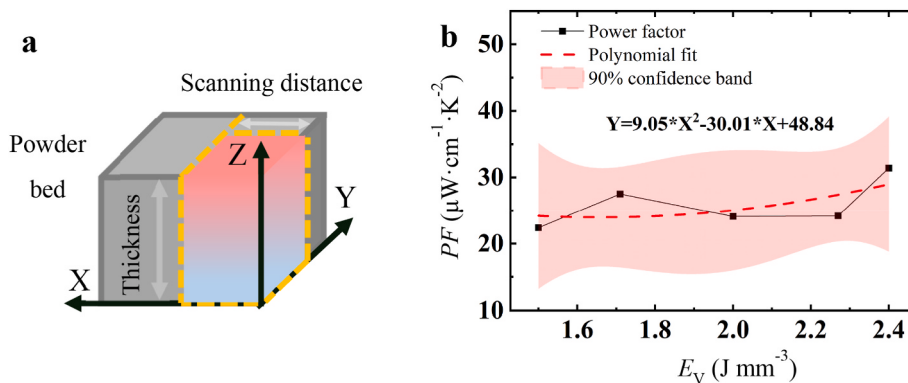


Fig. 5. **a**, Schematic of laser volumetric energy density. **b**, The volumetric energy density dependence of power factor. The dashed line and pink band indicate polynomial fit and 90 % confidence, respectively. (For interpretation of the references to colour in this figure legend, the reader is referred to the Web version of this article.)

direction appeared more concentrated, while it looked more dispersed in the other direction shown in Fig. 4 a₁ and Fig. 4 b₁. The electrical conductivity along the parallel direction was about two times higher than that in the perpendicular direction. The anisotropic electrical conductivity and thermopower were hypothetical owing to aligned grain microstructures of bismuth antimony telluride as presented in Fig. 3 c. Anisotropic differences were also characterized by power factors Fig. 4 a₃ and Fig. 4 b₃.

For the thermal conductivity in the two directions, there are minor differences within about 20 % in Fig. 4 a₄ and Fig. 4 b₄. Ultimately, the figure-of-merit zT values in parallel to the building direction were nearly three times as high as that in another direction because of the electrical and thermal transport properties, with the maximum zT values being 1.1 at 75 °C and 0.4 at 150 °C along parallel and perpendicular directions shown in Fig. 4 a₅ and Fig. 4 b₅.

To understand the effect of printing processes on TE performance, laser volumetric energy density E_V was accordingly investigated as a dependence on power factor PF . The variation of experimental value PF with E_V was fitted by a second-order polynomial. Their relationship was expressed as $PF = 9.05 E_V^2 - 30.01 E_V + 48.84$. The schematic of E_V in LPBF, fitting results, and 90 % confidence band are shown in Fig. 5. The 90 % confidence band was calculated according to estimated standard error, indicating a 90 % confidence that the best-fit line is located inside. Within the scope of the experimental research carried out, the PF was raised generally with the increase of E_V . The achieved peak PF of printed bulks was elevated to $31.4 \mu\text{W cm}^{-1}\text{K}^{-2}$, which was comparable to that of ingot [51].

The correlation between laser volumetric energy density E_V and electrical conductivity σ was specifically discussed to further explore the influence of input energy. According to Buckingham theorem, the relationship between E_V and density d of LPBF printed samples was obtained [55],

$$d_{\text{sample}} = \frac{CE_V}{v^2} \quad (1)$$

Where d_{sample} is the density of LPBF fabricated samples, C is a fitting

experimental parameter, and v is the scanning speed from the printing process. The fitting experimental parameter C owing to various LPBF process parameters was listed and compared in Table S4. Dimensionless C obtained an average value of 35.00×10^{-8} , and it was used in the calculations below.

According to the empirical formula of Langlois and Coeuret, the relationship between electrical conductivity σ and porosity ϵ is below [56],

$$\sigma_{\text{sample}} = \frac{1}{4}(1-\epsilon)\sigma_{\text{bulk}} \quad (2)$$

Where σ_{sample} and σ_{bulk} are the electrical conductivity of printed samples and dense bulks, respectively. The ϵ is the porosity of printed samples.

The porosity is expressed by the following formula [26,57],

$$\epsilon = \frac{V_{\text{pores}}}{V_{\text{bulk}}} = \frac{d_{\text{bulk}} - d_{\text{sample}}}{d_{\text{bulk}}} \quad (3)$$

where V_{pores} is defined as the volume of the pores in the sample and V_{bulk} as the nominal volume of the sample. The d_{bulk} denotes the density of bulk BST and its value is 6.73 g cm^{-3} [26]. The d_{sample} is the mass density of the sample that can be obtained using the Archimedes method. The porosity of different samples is shown in Table 1.

Substituting Eq. (1) and Eq. (3) into Eq. (2), thus Eq. (4) can be obtained,

$$\sigma_{\text{sample}} = K \frac{CE_V}{4v^2 d_{\text{bulk}}} \sigma_{\text{bulk}} \quad (4)$$

where K is a correction factor. The comparison of calculated and experimental results of electrical conductivity for LPBF-ed Bi_{0.5}Sb_{1.5}Te₃ samples parallel to the building direction was shown in Fig. S5. The experimental values were within the range of the calculated results. The calculated electrical conductivity increased with boosted E_V . Given the differences in laser volumetric energy density were small, the variations of calculated conductivity were also confined. Both weight density and electrical conductivity accordingly indicated laser energy dependence.

Table 1

Hall coefficient (R_H), carrier concentration (n), carrier mobility (μ), measured density (d), relative density (%), and porosity (%) of laser additive-manufactured samples along parallel building direction at room temperature.

Samples	S1-1.5	S2-1.7	S3-2.0	S4-2.3	S5-2.4
$R_H (\text{cm}^3\text{C}^{-1})$	$(2.05 \pm 0.05) \times 10^{-1}$	$(1.30 \pm 0.05) \times 10^{-1}$	$(4.02 \pm 0.05) \times 10^{-2}$	$(1.81 \pm 0.05) \times 10^{-3}$	$(5.62 \pm 0.05) \times 10^{-1}$
$n (\text{cm}^{-3})$	$(3.05 \pm 0.01) \times 10^{19}$	$(4.80 \pm 0.01) \times 10^{19}$	$(1.55 \pm 0.01) \times 10^{20}$	$(3.45 \pm 0.01) \times 10^{21}$	$(1.11 \pm 0.01) \times 10^{19}$
$\mu (\text{cm}^2\text{V}^{-1}\text{s}^{-1})$	$(1.42 \pm 0.11) \times 10^2$	$(1.01 \pm 0.11) \times 10^2$	$(2.56 \pm 0.11) \times 10^1$	$(1.23 \pm 0.11) \times 10^0$	$(4.89 \pm 0.11) \times 10^2$
$d (\text{g cm}^{-3})$	5.79 ± 0.03	6.06 ± 0.03	6.30 ± 0.03	6.50 ± 0.03	6.12 ± 0.03
Relative density (%)	$86.0 \% \pm 0.03$	$90.0 \% \pm 0.03$	$93.6 \% \pm 0.03$	$96.6 \% \pm 0.03$	$90.9 \% \pm 0.03$
Porosity (%)	$13.97 \% \pm 0.05$	$9.96 \% \pm 0.05$	$6.39 \% \pm 0.05$	$3.42 \% \pm 0.05$	$9.06 \% \pm 0.05$

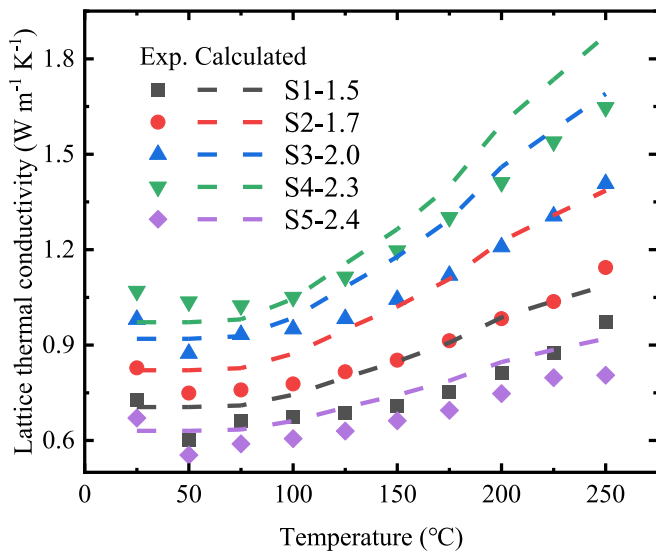


Fig. 6. Experimental (solid) and calculated (dash) lattice thermal conductivity of different printed BST samples as a function of temperature.

Therefore, the *PF* was able to be determined, even predicted based on the laser volumetric energy density E_V .

The charge carrier concentration, mobility, and density of the samples along parallel BD at room temperature were listed in Table 1. The hole carrier concentration varied with different process parameters from $3.45 \times 10^{21} \text{ cm}^{-3}$ to $1.11 \times 10^{19} \text{ cm}^{-3}$. Among all printed samples, the Hall coefficient and carrier concentration of sample S5-2.4 was closest to that of the corresponding ingot [58], which exhibited superior electrical transport properties. The highest carrier mobility improved the best figure of merit. The relative density of LPBF fabricated samples was about 90 %.

To further summarize the relationships of processing-microstructure-property of directly synthesized thermoelectric materials by laser printing, the volumetric energy density of LPBF is selected as a processing feature, and nanopores are considered as a microstructural character. The effect of nanopores on the lattice thermal conductivity of printed BST is calculated and analyzed.

The experimental lattice thermal conductivity of printed samples is estimated by subtracting the electrical thermal conductivity from the total thermal conductivity [9]. The electrical thermal conductivity is evaluated by the Wiedemann-Franz law $k_e = L\sigma T$, where L is the Lorenz number estimated by the $L = 1.5 + \exp(-|S|/116)$ [59], S is Seebeck coefficient, σ is electrical conductivity, and T is absolute temperature.

The lattice thermal conductivity k_{Lp} of printed BST is defined as the relation of the lattice thermal conductivity k_{Lb} of melted bulk after inducing nanopores. The k_{Lp} is calculated according to the “gray medium” approximation under the assumption of complete phonon scattering on the nanopore interfaces [60,61]:

$$k_{Lp} = \frac{1 - \varphi_n}{1 + \Lambda_b \left[\frac{3\alpha_n \varphi_n}{2(\alpha_n + 2)d_n} \right]} \times k_{Lb} \quad (5)$$

$$\varphi_n = \frac{1}{6} \pi c_n d_n^3 \left[\frac{(\alpha_n + 1)(\alpha_n + 2)}{\alpha_n^2} \right] \quad (6)$$

$$\Lambda_b = \frac{3k_{Lb}}{C_v v_a} \quad (7)$$

where k_{Lb} is the lattice thermal conductivity of melted bulk [62], α_n is the “shape” parameter of the gamma distribution and its value is set to 1 in this calculation, d_n is the average diameter of nanopores and its value is set as 50 nm [26], c_n is the number density of nanopores, Λ_b is the

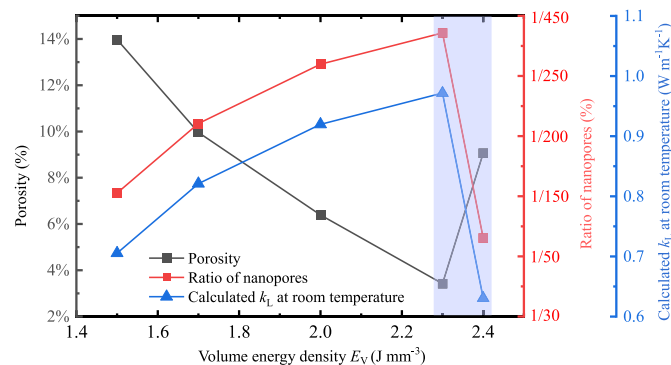


Fig. 7. Porosity, the ratio of nanopores, and calculated lattice thermal conductivity indicate dependence on the volume energy density of the laser at room temperature.

phonon mean free path, C_v is heat capacity determined by the Dulong-Petit law, v_a is the average sound velocity set as 2147 m s⁻¹ [63].

To determine c_n , the porosity of printed BST is first calculated according to mass density. Assuming the pores are well distributed, the porosity is a function of bulk density and the measured mass density of the porous sample in Table 1.

The number density of nanopores is defined below,

$$c_n = \frac{R_n \varepsilon}{\frac{4}{3} \pi (d_n)^3} \quad (8)$$

where R_n is the ratio of nanopores, ε is the porosity of printed samples.

According to the calculation of lattice thermal conductivity of printed BST, the ratio of nanopores is 1/150, 1/200, 1/300, 1/400, and 1/70 corresponding to samples S1-1.5, S2-1.7, S3-2.0, S4-2.3, and S5-2.4 respectively. The number density of associated nanopores c_n are 1.4×10^{19} , 7.6×10^{18} , 3.3×10^{18} , 1.3×10^{18} and 2.0×10^{19} m⁻³, respectively. Fig. 6 shows the experimental and calculated lattice thermal conductivity of different printed BST samples as a function of temperature, and it can be seen that the calculated results are in good agreement with the experimental results. Porosity, ratio of nanopores, and calculated lattice thermal conductivity at room temperature are functions of volume energy density as shown in Fig. 7. The E_V increased from 1.5 to 2.3 J mm⁻³, and the porosity decreased from 13.97 % to 3.42 % correspondingly because a higher laser energy density leads to more complete melting of thermoelectric materials, resulting in a denser material. Similarly, the ratio of nanopores decreased from 1/150 to 1/400. The porosity is reduced due to the preparation of dense thermoelectric materials due to high energy density. The number density of nanopores also decreased from 1.4×10^{19} to 1.3×10^{18} m⁻³. The lattice thermal conductivity at room temperature is analyzed as a typical case. It is well known that the low lattice thermal conductivity is caused by the effective phonon scattering at induced nanopores [51,54]. Therefore, the higher the number density of nanopores from 1.4×10^{19} to 1.3×10^{18} m⁻³, the lower the lattice thermal conductivity from 0.71 to 0.97 W m⁻¹ K⁻¹.

Interestingly, when the laser volume energy density E_V increases up to 2.4 J mm⁻³, the porosity does not continue to decrease but increases to 9.06 %. Therefore, the change in laser energy density E_V from 2.3 to 2.4 J mm⁻³ is a critical turning point for bismuth telluride thermoelectric materials. This may be because bismuth telluride and some elemental element powders are volatilized by the volume energy density exceeding the critical point, increasing the number density of nanopores. Comparable phenomena and experimental results were reported to confirm induced nanopore structures by high energy processing process [26,64].

Note that the strong phonon scattering triggered by lattice distortion could also limit the thermal conductivity. As shown in Fig. S6, the

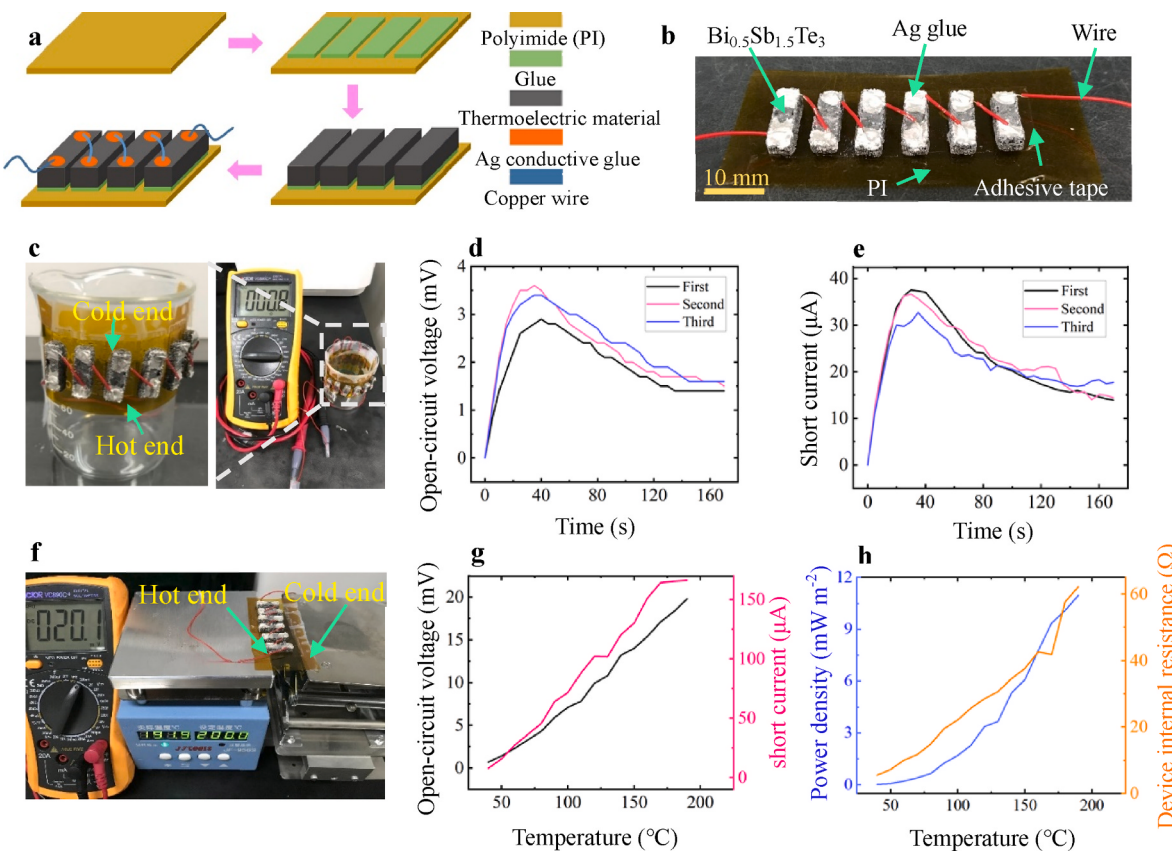


Fig. 8. Output performance of unidirectional flexible TE device. **a**, Schematic diagram of the fabrication process. **b**, Photograph of 6 single p-type $\text{Bi}_{0.5}\text{Sb}_{1.5}\text{Te}_3$ legs. **c-e**, TE device placed on a beaker with a portion of boiling water and time-dependent open-circuit voltage and short current. **f-h**, TE device placed on a hot plate with different temperatures and its corresponding performance.

thermal conductivity of most LPBF printed samples in both parallel and perpendicular directions is much lower than that of the melted bulks [50]. Chen et al. also reported that lattice distortions play a positive role in reducing the thermal conductivity of polycrystalline Bi_2Te_3 [65]. Furthermore, as the energy E_V increases, the thermal conductivity first increases and then decreases along both parallel and vertical directions (Fig. S7). The laser energy dependence of element composition and mass density were quantified in Fig. S8.

Flexible TE devices with directly printed materials were schematically illustrated in Fig. 8 a. A TE device consisting of 6 legs with a three-dimensional size of $5 \times 5 \times 12$ mm was fabricated to quantify thermoelectric performance (Fig. 8 b). Two application scenarios were demonstrated, one example was the TE device applied on a beaker with a portion of boiling water, the hot end was provided by the liquid level of boiling water, and the cold end was in the air environment, Fig. 8 c. It could be seen from Fig. 8 d-e that the output performance shows good repeatability. Another demo was the device placed on a hot plate with different temperatures, which was used as a hot source. The cold end was similar in air condition and its output performances were presented as shown in Fig. 8 f-h.

In the future, the carrier concentration will be tuned to print high-performance bulk raw materials in the guidance of reverse design strategies. Both spherical *p*-type and *n*-type bismuth telluride particles should be considered to improve printing quality, such as dimensional accuracy and surface roughness of TE legs.

4. Conclusions

In our work, *p*-type $\text{Bi}_{0.5}\text{Sb}_{1.5}\text{Te}_3$ polycrystalline bulks with high TE properties are directly and massively synthesized by laser powder bed fusion (LPBF) additive manufacturing techniques from a mixture of Bi,

Sb, and Te individual powders, and designed dimensions are simultaneously shaped. Significant anisotropy of thermoelectric performance is characterized and analyzed as a result of aligned polycrystal microstructures. The correlation between power factor PF along building direction and laser volumetric energy density E_V is achieved, $PF = 9.05 \cdot E_V^2 - 30.01 \cdot E_V + 48.84$, leading to a predictable thermoelectric performance based on input laser power. This correlation is also critical for TE materials and device design to achieve fine performance using specific laser power. The maximum zT value of 1.1 at 75°C without any pre- and post-processing is accomplished along the building direction, sourced from the high power factor of $29.5 \mu\text{W cm}^{-1} \text{K}^{-2}$ and low total thermal conductivity of $0.9 \text{ W m}^{-1} \text{ K}^{-1}$. To summarize the relationships of processing-microstructure-property of directly synthesized bismuth telluride thermoelectric materials by LPBF, nanopores are considered as a microstructural character. Nanopores are fabricated due to tellurium evaporation, especially at high laser power levels. The average diameter of nanopores is comparable to the phonon mean free path, leading to reduced lattice thermal conductivity and enhanced thermoelectric performance.

Declaration of competing interest

The authors declare that they have no known competing financial interests or personal relationships that could have appeared to influence the work reported in this paper.

Acknowledgments

The authors would like to acknowledge the financial support from the National Natural Science Foundation of China (grant number: 52175248), the State Key Laboratory for Manufacturing Systems

Engineering open fund (grant number: sklms2022001), and the Key R&D Program of Shannxi, China (grant number: 2023-YBGF-358). The authors thank the Instrument Analysis Center of Xi'an Jiaotong University for the assistance with TEM analysis. The authors thank Shenzhen Key Laboratory of Thermoelectric Materials at Southern University of Science and Technology (SUSTech) for thermoelectric properties measurement.

Appendix A. Supplementary data

Supplementary data to this article can be found online at <https://doi.org/10.1016/j.ceramint.2023.11.035>.

References

- [1] Z. Zheng, X. Shi, D. Ao, W. Liu, M. Li, L. Kou, Y. Chen, F. Li, M. Wei, G. Liang, P. Fan, G. Lu, Z. Chen, Harvesting waste heat with flexible Bi₂Te₃ thermoelectric thin film, *Nat. Sustain.* 6 (2) (2023) 180–191.
- [2] X. Shi, J. Zou, Z. Chen, Advanced thermoelectric design: from materials and structures to devices, *Chem. Rev.* 120 (15) (2020) 7399–7515.
- [3] W. Chen, X. Shi, J. Zou, Z. Chen, Thermoelectric coolers for on-chip thermal management: materials, design, and optimization, *Mater. Sci. Eng. R Rep.* 151 (2022), 100700.
- [4] J. He, T. Tritt, Advances in thermoelectric materials research: looking back and moving forward, *Science* 357 (6358) (2017), eaak9997.
- [5] J. Mao, High thermoelectric cooling performance of n-type Mg₃Bi₂-based materials, *Science* 365 (6452) (2019) 495–498.
- [6] B. Jiang, W. Wang, S. Liu, Y. Wang, C. Wang, Y. Chen, L. Xie, M. Huang, J. He, High figure-of-merit and power generation in high-entropy GeTe-based thermoelectrics, *Science* 377 (6602) (2022) 208–213.
- [7] B. Zhu, W. Wang, J. Cui, J. He, Point defect engineering: Co-doping synergy realizing superior performance in n-type Bi₂Te₃ thermoelectric materials, *Small* 17 (29) (2021), 2101328.
- [8] B. Jia, Y. Huang, Y. Wang, Y. Zhou, X. Zhao, S. Ning, X. Xu, P. Lin, Z. Chen, B. Jiang, J. He, Realizing high thermoelectric performance in non-nanostructured n-type PbTe, *Energy Environ. Sci.* 15 (5) (2022) 1920–1929.
- [9] B. Zhu, X. Liu, Q. Wang, Y. Qiu, Z. Shu, Z. Guo, Y. Tong, J. Cui, M. Gu, J. He, Realizing record high performance in n-type Bi₂Te₃-based thermoelectric materials, *Energy Environ. Sci.* 13 (7) (2020) 2106–2114.
- [10] X. Xu, J. Cui, Y. Yu, B. Zhu, Y. Huang, L. Xie, D. Wu, J. He, Constructing van der Waals gaps in cubic-structured SnTe-based thermoelectric materials, *Energy Environ. Sci.* 13 (12) (2020) 5135–5142.
- [11] Y. Lu, Y. Qiu, K. Cai, X. Li, M. Gao, C. Jiang, J. He, Ultrahigh performance PEDOT/Ag₂Se/CuAgSe composite film for wearable thermoelectric power generators, *Mater. Today Phys.* 14 (2020), 100223.
- [12] C. Chang, M. Wu, D. He, Y. Pei, C. Wu, X. Wu, H. Yu, F. Zhu, K. Wang, Y. Chen, L. Huang, J. Li, J. He, L. Zhao, 3D charge and 2D phonon transports leading to high out-of-plane ZT in n-type SnSe crystals, *Science* 360 (6390) (2018) 778–782.
- [13] G. Snyder, Complex thermoelectric materials, *Nat. Mater.* 7 (2) (2008) 105–114.
- [14] X. Shi, W. Liu, M. Li, Q. Sun, S. Xu, D. Du, J. Zou, Z. Chen, A Solvothermal synthetic environmental design for high-performance SnSe-based thermoelectric materials, *Adv. Energy Mater.* 12 (20) (2022), 2200670.
- [15] W. Hao, X. Shi, J. Duan, Q. Liu, Z. Chen, Advances in Ag₂Se-Based Thermoelectrics from Materials to Applications, *Energy & Environmental Science*, 2023.
- [16] N. Chen, H. Zhu, G. Li, Z. Fan, X. Zhang, J. Yang, T. Lu, Q. Liu, X. Wu, Y. Yao, Y. Shi, H. Zhao, Improved figure of merit (α) at low temperatures for superior thermoelectric cooling in Mg₃(Bi, Sb)₂, *Nat. Commun.* 14 (1) (2023) 4932.
- [17] Q. Dong, J. Xiang, Z. Wang, Y. Li, R. Lu, T. Zhang, N. Chen, Y. Huang, Y. Wang, W. Zhu, G. Li, H. Zhao, X. Zheng, S. Zhang, Z. Ren, J. Yang, G. Chen, P. Sun, A quasi-one-dimensional bulk thermoelectrics with high performance near room temperature, *Sci. Bull.* 68 (9) (2023) 920–927.
- [18] X. Shi, Z. Chen, Quasi-one-dimensional bulk thermoelectrics, *Joule* 7 (6) (2023) 1108–1110.
- [19] S. Sun, M. Li, X. Shi, Z. Chen, Advances in ionic thermoelectrics: from materials to devices, *Adv. Energy Mater.* 13 (9) (2023), 2203692.
- [20] W. Chen, X. Shi, J. Zou, Z. Chen, Wearable fiber-based thermoelectrics from materials to applications, *Nano Energy* 81 (2021), 105684.
- [21] D. Ao, W. Liu, Y. Chen, M. Wei, B. Jabar, F. Li, X. Shi, Z. Zheng, G. Liang, X. Zhang, P. Fan, Z. Chen, Novel thermal diffusion temperature engineering leading to high thermoelectric performance in Bi₂Te₃-based flexible thin-films, *Adv. Sci.* 9 (5) (2022), 2103547.
- [22] S. LeBlanc, Thermoelectric generators: linking material properties and systems engineering for waste heat recovery applications, *Sustain. Mater. Tech.* 1 (2014) 26–35.
- [23] J. Martin, B. Yahata, J. Hundley, J. Mayer, T. Schaedler, T. Pollock, 3D printing of high-strength aluminium alloys, *Nature* 549 (7672) (2017) 365–369.
- [24] L. Zhang, J. Lifton, Z. Hu, R. Hong, S. Feih, Influence of geometric defects on the compression behaviour of thin shell lattices fabricated by micro laser powder bed fusion, *Addit. Manuf.* 58 (2022), 103038.
- [25] M. Yan, X. Tian, G. Peng, D. Li, X. Zhang, High temperature rheological behavior and sintering kinetics of CF/PEEK composites during selective laser sintering, *Compos. Sci. Technol.* 165 (2018) 140–147.
- [26] J. Shi, H. Chen, S. Jia, W. Wang, 3D printing fabrication of porous bismuth antimony telluride and study of the thermoelectric properties, *J. Manuf. Process.* 37 (2019) 370–375.
- [27] H. Chen, W. Zhu, H. Tang, W. Yan, Oriented structure of short fiber reinforced polymer composites processed by selective laser sintering: the role of powder spreading process, *Int. J. Mach. Tool Manufact.* 163 (2021), 103703.
- [28] M. Izadi, A. Farzaneh, M. Mohammed, I. Gibson, B. Rolfe, A review of laser engineered net shaping (LENS) build and process parameters of metallic parts, *Rapid Prototyp. J.* 26 (6) (2020) 1059–1078.
- [29] D. Gu, X. Shi, R. Poprawe, D.L. Bourell, R. Setchi, J. Zhu, Material-structure-performance integrated laser-metal additive manufacturing, *Science* 372 (6545) (2021), eabg1487.
- [30] J. Ren, Y. Zhang, D. Zhao, Y. Chen, S. Guan, Y. Liu, L. Liu, S. Peng, F. Kong, J. D. Poplawsky, G. Gao, T. Voisin, K. An, Y.M. Wang, K.Y. Xie, T. Zhu, W. Chen, Strong yet ductile nanolamellar high-entropy alloys by additive manufacturing, *Nature* 608 (7921) (2022) 62–68.
- [31] Z. Xiong, H. Li, H. Yang, Y. Yang, Y. Liu, L. Cui, X. Li, L. Masseling, L. Shen, S. Hao, Micro laser powder bed fusion of NiTi alloys with superior mechanical property and shape recovery function, *Addit. Manuf.* 57 (2022), 102960.
- [32] C. Wei, L. Liu, Y. Gu, Y. Huang, Q. Chen, Z. Li, L. Li, Multi-material additive-manufacturing of tungsten - copper alloy bimetallic structure with a stainless-steel interlayer and associated bonding mechanisms, *Addit. Manuf.* 50 (2022), 102574.
- [33] A. El-Dessouky, M. Carter, M.A. Andre, P.M. Bardet, S. LeBlanc, Rapid processing and assembly of semiconductor thermoelectric materials for energy conversion devices, *Mater. Lett.* 185 (2016) 598–602.
- [34] A. El-Dessouky, M. Carter, M. Mahmoudi, A. Elwany, S. LeBlanc, Influences of energy density on microstructure and consolidation of selective laser melted bismuth telluride thermoelectric powder, *J. Manuf. Process.* 25 (2017) 411–417.
- [35] M. Carter, A. El-Dessouky, M. Andre, P. Bardet, S. LeBlanc, Pulsed laser melting of bismuth telluride thermoelectric materials, *J. Manuf. Process.* 43 (2019) 35–46.
- [36] H. Zhang, D. Hobbs, G.S. Nolas, S. LeBlanc, Laser additive manufacturing of powdered bismuth telluride, *J. Mater. Res.* 33 (23) (2018) 4031–4039.
- [37] Y. Mao, Y. Yan, K. Wu, H. Xie, Z. Xiu, J. Yang, Q. Zhang, C. Uher, X. Tang, Non-equilibrium synthesis and characterization of n-type Bi₂Te_{2.7}Se_{0.3} thermoelectric material prepared by rapid laser melting and solidification, *RSC Adv.* 7 (35) (2017) 21439–21445.
- [38] J. Qiu, Y. Yan, T. Luo, K. Tang, L. Yao, J. Zhang, M. Zhang, X. Su, G. Tan, H. Xie, M. Kanatzidis, C. Uher, X. Tang, 3D printing of highly textured bulk thermoelectric materials: mechanically robust Bi₂Te₃ alloys with superior performance, *Energy Environ. Sci.* 12 (10) (2019) 3106–3117.
- [39] H. Zhang, S. LeBlanc, Laser additive manufacturing process development for bismuth telluride thermoelectric material, *J. Mater. Eng. Perform.* 31 (8) (2022) 6196–6204.
- [40] J. Shi, X. Chen, W. Wang, H. Chen, A new rapid synthesis of thermoelectric Sb₂Te₃ ingots using selective laser melting 3D printing, *Mater. Sci. Semicond. Process.* 123 (2021), 105551.
- [41] R. Zhan, J. Lyu, D. Yang, Y. Liu, S. Hua, Z. Xu, C. Wang, X. Peng, Y. Yan, X. Tang, Large-scale SHS based 3D printing of high-performance n-type Bi₂Te₃: comprehensive development from materials to modules, *Mater. Today Phys.* 24 (2022), 100670.
- [42] Y. Thimont, L. Presmanes, V. Baylac, P. Tailhades, D. Berthebaud, F. Gascoin, Thermoelectric Higher Manganese Silicide: synthetized, sintered and shaped simultaneously by selective laser sintering/Melting additive manufacturing technique, *Mater. Lett.* 214 (2018) 236–239.
- [43] C. Luo, J. Qiu, Y. Yan, J. Yang, C. Uher, X. Tang, Finite element analysis of temperature and stress fields during the selective laser melting process of thermoelectric SnTe, *J. Mater. Process. Technol.* 261 (2018) 74–85.
- [44] T. Chen, C. Luo, Y. Yan, J. Yang, Q. Zhang, C. Uher, X. Tang, Rapid fabrication and thermoelectric performance of SnTe via non-equilibrium laser 3D printing, *Rare Met.* 37 (4) (2018) 300–307.
- [45] Y. Yan, H. Ke, J. Yang, C. Uher, X. Tang, Fabrication and thermoelectric properties of n-type CoSb_{2.5}Te_{0.15} using selective laser melting, *ACS Appl. Mater. Interfaces* 10 (16) (2018) 13669–13674.
- [46] H. Zhang, S. Wang, P. Taylor, J. Yang, S. LeBlanc, Selective laser melting of half-heusler thermoelectric materials, energy harvesting and storage: materials, devices, and applications VIII, SPIEL 10663 (2018) 10–17.
- [47] Y. Yan, W. Geng, J. Qiu, H. Ke, C. Luo, J. Yang, C. Uher, X. Tang, Thermoelectric properties of n-type ZrNiSn prepared by rapid non-equilibrium laser processing, *RSC Adv.* 8 (28) (2018) 15796–15803.
- [48] Y. Kinemuchi, M. Mikami, I. Terasaki, W. Shin, Rapid synthesis of thermoelectric compounds by laser melting, *Mater. Des.* 106 (2016) 30–36.
- [49] C. Oztan, R. Welch, S. LeBlanc, Additive manufacturing of bulk thermoelectric architectures: a review, *Energies* 15 (9) (2022) 3121.
- [50] B. Poudel, Q. Hao, Y. Ma, Y.C. Lan, A. Minnich, B. Yu, X.A. Yan, D.Z. Wang, A. Muto, D. Vashaei, X.Y. Chen, J.M. Liu, M.S. Dresselhaus, G. Chen, Z.F. Ren, High-thermoelectric performance of nanostructured bismuth antimony telluride bulk alloys, *Science* 320 (5876) (2008) 634–638.
- [51] S. Kim, K. Lee, H. Mun, H. Kim, S. Hwang, J. Roh, D. Yang, W. Shin, X. Li, Y. Lee, G. Snyder, S. Kim, Dense dislocation arrays embedded in grain boundaries for high-performance bulk thermoelectrics, *Science* 348 (6230) (2015) 109–114.
- [52] Y. Mao, Y. Yan, K. Wu, H. Xie, Z. Xiu, J. Yang, Q. Zhang, C. Uher, X. Tang, Non-equilibrium synthesis and characterization of n-type Bi₂Te_{2.7}Se_{0.3} thermoelectric material prepared by rapid laser melting and solidification, *RSC Adv.* 7 (35) (2017) 21439–21445.

- [53] D. Bao, J. Chen, Y. Yu, W. Liu, L. Huang, G. Han, J. Tang, D. Zhou, L. Yang, Z. Chen, Texture-dependent thermoelectric properties of nano-structured Bi₂Te₃, *Chem. Eng. J.* 388 (2020), 124295.
- [54] H. Zhang, C. Li, G. Yao, Y. Shi, Y. Zhang, Effect of annealing treatment on microstructure evolution and deformation behavior of 304 L stainless steel made by laser powder bed fusion, *Int. J. Plast.* 155 (2022), 103335.
- [55] J. Estrada-Diaz, A. Elias-Zuniga, O. Martinez-Romero, J. Rodriguez-Salinas, D. Olvera-Trejo, A mathematical dimensional model for predicting bulk density of inconel 718 parts produced by selective laser melting, *Materials* 14 (3) (2021) 512.
- [56] M. Mustapha, F. Ismail, O. Mamat, Empirical relationship between relative electrical conductivity and relative density of the Al-foam fabricated through pressure assisted sintering/dissolution process, *IOP Conf. Ser. Mater. Sci. Eng.* 17 (2011), 012014.
- [57] W. Yeong, N. Sudarmadji, H. Yu, C. Chua, K. Leong, S. Venkatraman, Y. Boey, L. Tan, Porous polycaprolactone scaffold for cardiac tissue engineering fabricated by selective laser sintering, *Acta Biomater.* 6 (6) (2010) 2028–2034.
- [58] B. Madavali, H. Kim, K. Lee, Y. Isoda, F. Gascoin, S. Hong, Large scale production of high efficient and robust p-type Bi-Sb-Te based thermoelectric materials by powder metallurgy, *Mater. Des.* 112 (2016) 485–494.
- [59] H. Kim, Z. Gibbs, Y. Tang, H. Wang, G. Snyder, Characterization of Lorenz number with Seebeck coefficient measurement, *Apl. Mater.* 3 (4) (2015).
- [60] X. Shi, A. Wu, W. Liu, R. Moshwan, Y. Wang, Z. Chen, J. Zou, Polycrystalline SnSe with extraordinary thermoelectric property via nanoporous design, *ACS Nano* 12 (11) (2018) 11417–11425.
- [61] R. Tarkhanyan, D. Niarchos, Reduction of thermal conductivity in porous “gray” materials, *Apl. Mater.* 2 (7) (2014).
- [62] Q. Zhang, G. Wu, Z. Guo, P. Sun, R. Wang, L. Chen, X. Wang, X. Tan, H. Hu, B. Yu, J. Noudem, G. Liu, J. Jiang, Enhanced thermoelectric and mechanical performances in sintered Bi_{0.48}Sb_{1.52}Te₃–AgSbSe₂ composite, *ACS Appl. Mater. Interfaces* 13 (21) (2021) 24937–24944.
- [63] Y. Wang, W. Liu, H. Gao, L. Wang, M. Li, X. Shi, M. Hong, H. Wang, J. Zou, Z. Chen, High porosity in nanostructured n-type Bi₂Te₃ obtaining ultralow lattice thermal conductivity, *ACS Appl. Mater. Interfaces* 11 (34) (2019) 31237–31244.
- [64] T. Yamamoto, M. Hara, Y. Hatano, Effects of fabrication conditions on the microstructure, pore characteristics and gas retention of pure tungsten prepared by laser powder bed fusion, *Int. J. Refract. Metals Hard Mater.* 95 (2021), 105410.
- [65] W. Chen, X. Shi, Q. Yang, M. Li, W. Lyu, T. Liu, T. Cao, B. Hu, W. Liu, S. Sun, Y. Mao, M. Dargusch, J. Zou, Z. Chen, Solvothermally silver doping boosting the thermoelectric performance of polycrystalline Bi₂Te₃, *Chem. Eng. J.* 475 (2023), 146428.

1 ***Supplementary Information***

2

3 **Predictable thermoelectric performance of directly synthesized**
4 **Bi_{0.5}Sb_{1.5}Te₃ using laser powder bed fusion additive manufacturing**

5 Jianxu Shi^{1, 2, a}, Zhiqiang Tong^{2, a}, Chunjiang Wang², Bobo Li^{3, 4}, Shengli Cao¹, Yihui
6 Hu¹, Zhicang Wang¹, Jun Peng^{3*}

7 ¹ School of Automation, Xi'an University of Posts and Telecommunications, Xi'an
8 Shaanxi, 710121, China

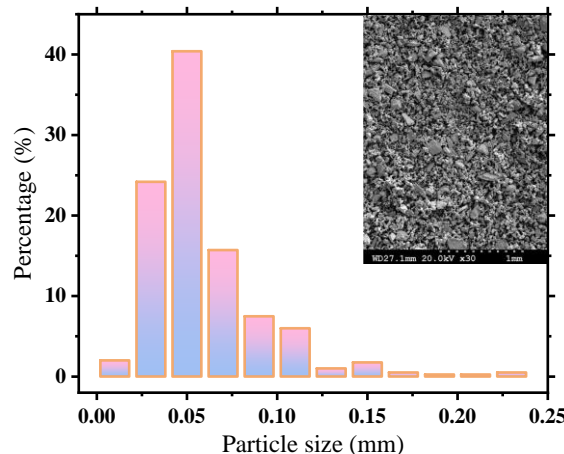
9 ² State Key Laboratory for Manufacturing Systems Engineering, Xi'an Jiaotong
10 University, Xi'an, Shaanxi, 710049, China

11 ³ School of Mechanical Engineering, Xi'an Jiaotong University, Xi'an, Shaanxi, 710049,
12 China

13 ⁴ National Innovation Institute of Additive Manufacturing, No. 997, Shanglinyuan 8th
14 Road, Gaoxin District, Xi'an 710300, China

15 * Corresponding author. E-mail address: pengjun@xjtu.edu.cn

16 ^a These authors contributed equally to this work.



19 **Fig. S1.** Size distribution of three elemental powders Bi, Sb and Te mixed powders according to
20 stoichiometric ratio Bi_{0.5}Sb_{1.5}Te₃ and excess 5 wt% Te. The corresponding SEM image in upper
21 right corner showing powder morphology.

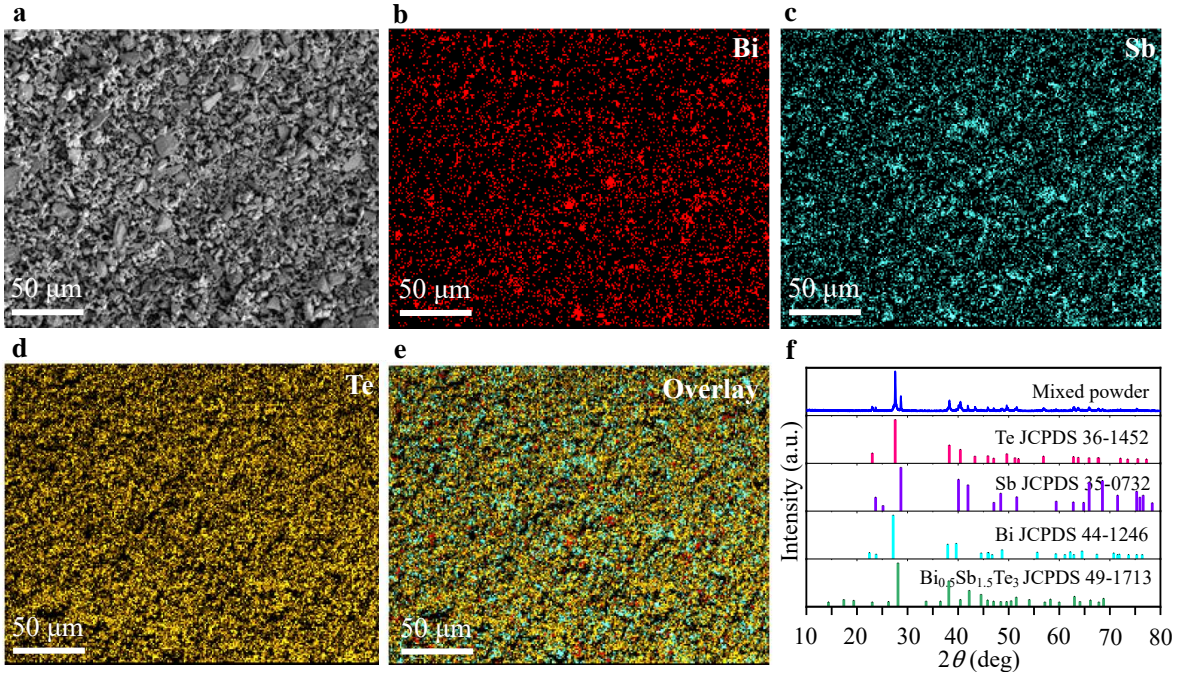


Fig. S2. Structural characterization of three elemental powders Bi, Sb, and Te mixed powders according to stoichiometric ratio $\text{Bi}_{0.5}\text{Sb}_{1.5}\text{Te}_3$ and excess 5 wt% Te. **a**, SEM. **b-e**, EDS mapping of Bi, Sb, Te, and overlay. **f**, XRD of mixture powders.

LPBF features large temperature gradients and rapid temperature changes [1], for instance, $10^5\text{-}10^7\text{ }^\circ\text{C s}^{-1}$, which is difficult to directly observe experimentally. Therefore, simulating its manufacturing process with corresponding experimental means helps to understand the additive manufacturing process and the physical/chemical changes. **Fig. S3** illustrates the experiment of laser-additive manufactured Bi, Sb, and Te mixture powder by thermogravimetric analysis (TGA)-differential scanning calorimeter (DSC). The TGA and DSC curves with temperature from $30\text{ }^\circ\text{C}$ to $680\text{ }^\circ\text{C}$ at different heating rates of $10, 30, 50, 70$, and $100\text{ }^\circ\text{C min}^{-1}$ are shown in **Fig. S3 a** and **b**. As can be seen from TGA and DSC figures, the curve changes more and more consistently as the heating rate increases, especially at a heating rate of $70\text{ }^\circ\text{C min}^{-1}$. There are three exothermic peaks and two endothermic peaks at the heating rate in **Fig. S3 c**. Some special temperature points are selected according to the positions of exothermic and endothermic peaks. The mixed Bi, Sb, and Te mixture powder is heated to $200\text{ }^\circ\text{C}$, $450\text{ }^\circ\text{C}$, $530\text{ }^\circ\text{C}$, and $680\text{ }^\circ\text{C}$ with a heating rate of $70\text{ }^\circ\text{C min}^{-1}$. The phase and crystal structure of these heated powder are analyzed separately by XRD. The individual XRD patterns are shown in **Fig. S4**. According to the phase diagram of Bi/Sb/Te and the physical properties of corresponding alloys, the melting points of Bi, Sb, Te, Bi_2Te_3 , Sb_2Te_3 , and $\text{Bi}_{0.5}\text{Sb}_{1.5}\text{Te}_3$ are $271.5\text{ }^\circ\text{C}$, $630.6\text{ }^\circ\text{C}$, $449.6\text{ }^\circ\text{C}$, $580\text{ }^\circ\text{C}$, $617.7\text{ }^\circ\text{C}$, and about $580\text{ }^\circ\text{C}$, respectively. When heated to $200\text{ }^\circ\text{C}$, the temperature is below the melting point

45 of Bi, Sb, and Te, the exothermic peaks at 84.8 °C correspond to a solid-state reaction
 46 of Bi, Sb, and Te, which generates trace amounts of Bi₂Te₃, Sb₂Te₃, and Bi_{0.5}Sb_{1.5}Te₃.
 47 When heated to 450 °C, a weak endothermic peak at 269.1 °C is indexed as the eutectic
 48 point of Bi and Bi₂Te₃/Sb₂Te₃, the exothermic peak at 403.4 °C indicates further
 49 alloying of a small amount of Bi₂Te₃/Sb₂Te₃ and Bi_{0.5}Sb_{1.5}Te₃. When heated to 530 °C,
 50 the exothermic peak at 518.9 °C corresponds to further alloying of a considerable
 51 amount of Bi_{0.5}Sb_{1.5}Te₃. When heated to 680 °C, the endothermic peak at 599.4 °C may
 52 be indexed as the eutectic point of Bi_{0.5}Sb_{1.5}Te₃ and Sb. The proximate single phase of
 53 Bi_{0.5}Sb_{1.5}Te₃ is achieved when the mixture powder is heated to around 680 °C.

54 Laser volumetric energy density in LPBF [2],
 55

$$E_V = \frac{P}{vdt} \quad (1)$$

56 Where P is the laser power (W), v is the scanning speed (mm/s), d is the scanning
 57 spacing (mm), and t is the thickness (mm) of the powder bed.
 58

59 **Table S1.** Process parameters for LPBF of Bi, Sb, Te mixture and its calculated energy density.

Sample number	Power (W)	Scanning speed (mm·s ⁻¹)	Scanning distance (mm)	Areal energy density (J·mm ⁻²)	Volumetric energy density (J·mm ⁻³)
S1-1.5	60	400	0.05	2.39	1.5
S2-1.7	60	350	0.05	2.73	1.71
S3-2.0	60	300	0.05	3.18	2
S4-2.3	68	300	0.05	3.61	2.27
S5-2.4	60	250	0.05	3.82	2.4

60
 61
 62
 63
 64
 65
 66
 67
 68
 69
 70

71

Table S2. The calculation of synthesis rate in different methods.

Synthesis method	Synthesis rate (g h ⁻¹)	Synthesis time	Ref.
Melting	100	10 h at 1073 K, about 100g*10	[3]
Zone melting	30.77	10 h at 1073 K, a growth rate of 8 mm/h, about 4 cm long tapers, length 18 cm	[4]
Ball milling	3.3	rotational speed of 150 rpm for 30 h	[5]
High pressure	10	25 min at 930 K for general 4 or 5 g	[6]
Microwave solvothermal	12	microwave oven at 230 °C for 5 min, about 1000 mg	[7]
This work	254	6 mm × 6 mm × 2 mm can be printed out within 6 seconds	

72

73
74**Table S3.** Energy dispersive X-ray microanalysis of laser additive-manufactured samples from SEM-EDS.

Element	Designed atomic percent	Sample number and tested percentage				
		S1-1.5	S2-1.7	S3-2.0	S4-2.3	S5-2.4
Bi	10	8.72	8.68	10.64	10.64	8.35
Sb	30	36.32	32.51	33.89	30.90	35.76
Te	60	54.95	58.80	55.47	58.46	55.89

75

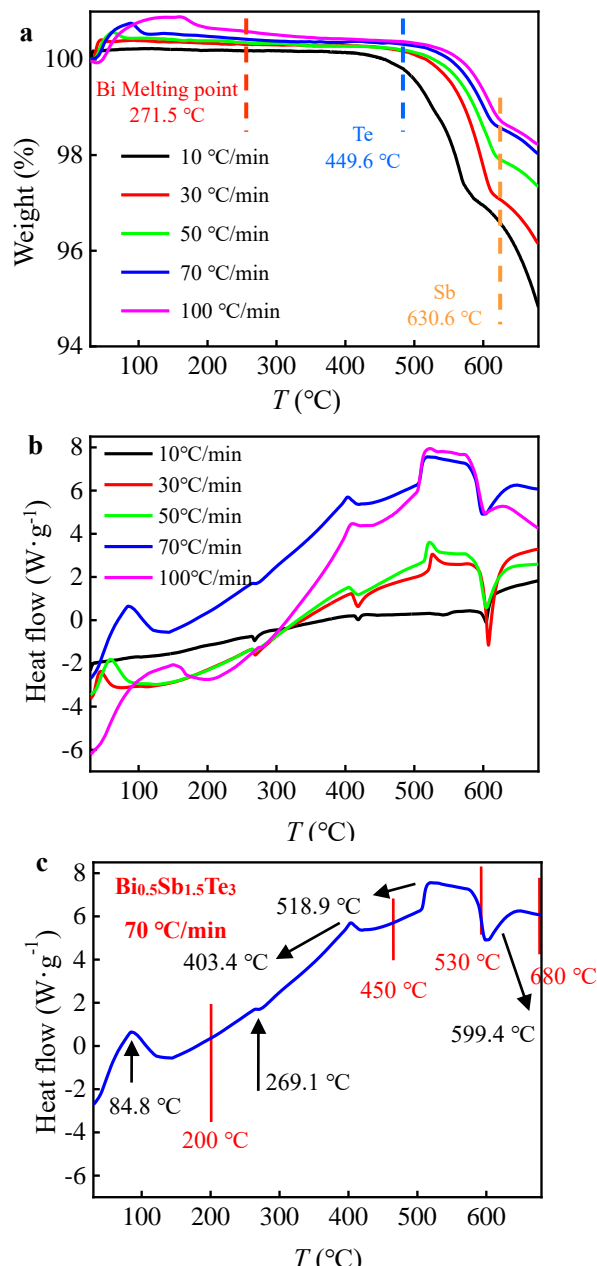
76

Table S4. Fitting experimental parameter C.

Samples	S1-1.5	S2-1.7	S3-2.0	S4-2.3	S5-2.4
C ($\times 10^{-8}$)	61.76	43.66	28.64	25.00	15.94

77

78



79

80 **Fig. S3.** TGA-DSC thermogram of Bi, Sb, and Te elemental mixture at different heating rates. **a**
 81 and **b**, Thermogravimetric variation and heat flow with temperature at different heating rates. **c**,
 82 Heat flow with temperature at a heating rate of $70 \text{ }^{\circ}\text{C} \cdot \text{min}^{-1}$.

83

84

85

86

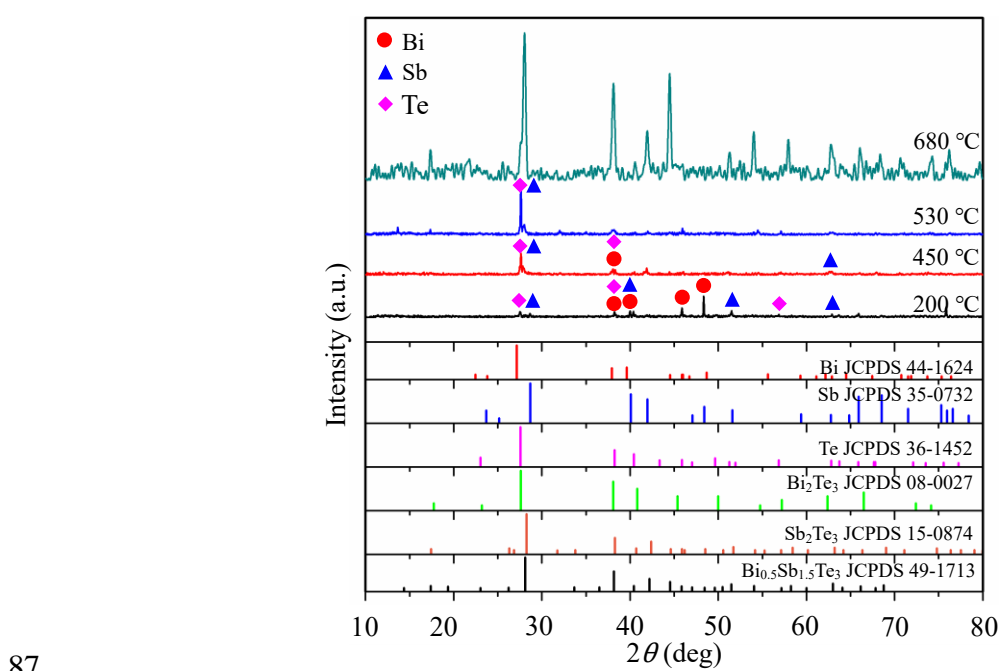
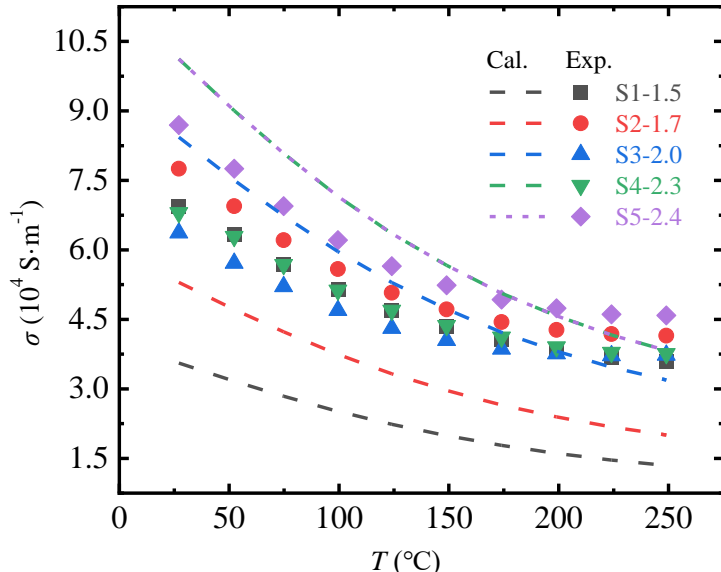


Fig. S4. XRD patterns of the products of Bi, Sb, and Te elemental mixture heated to different temperatures at a heating rate of $70 \text{ }^{\circ}\text{C} \cdot \text{min}^{-1}$

91

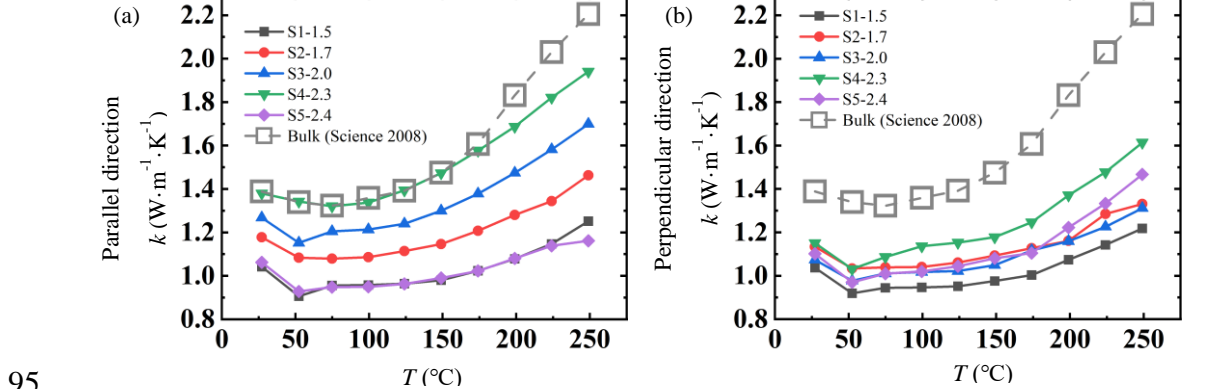


92

Fig. S5. Calculation and experimental value of electrical conductivity for LPBF-ed $\text{Bi}_{0.5}\text{Sb}_{1.5}\text{Te}_3$ materials parallel to the building direction

93

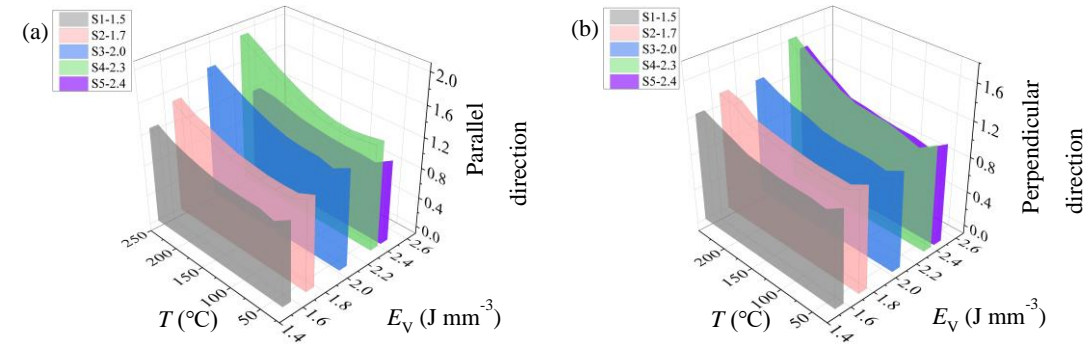
94



95

96 **Fig. S6.** Comparison of thermal conductivity of LPBF printed samples in parallel (a) and
97 perpendicular (b) directions to that of melted bulk.

98



99 **Fig. S7.** Temperature of thermal conductivity of samples synthesized by LPBF
100 printing in parallel (a) and perpendicular (b) directions under different volumetric
101 energy density E_V .

102 From another perspective of printed composition to summarize the relationships
103 of processing-microstructure-property of directly synthesized thermoelectric materials
104 by laser printing, the composition of the printed sample, indicated by EDS, is
105 considered as a microstructural character. Specifically, the relative value of the designed
106 atomic percent minus the tested EDS element percentage of printed samples is defined
107 as an indicator. The calculation relationship of cumulative deviation (Tot) is as follows,
108

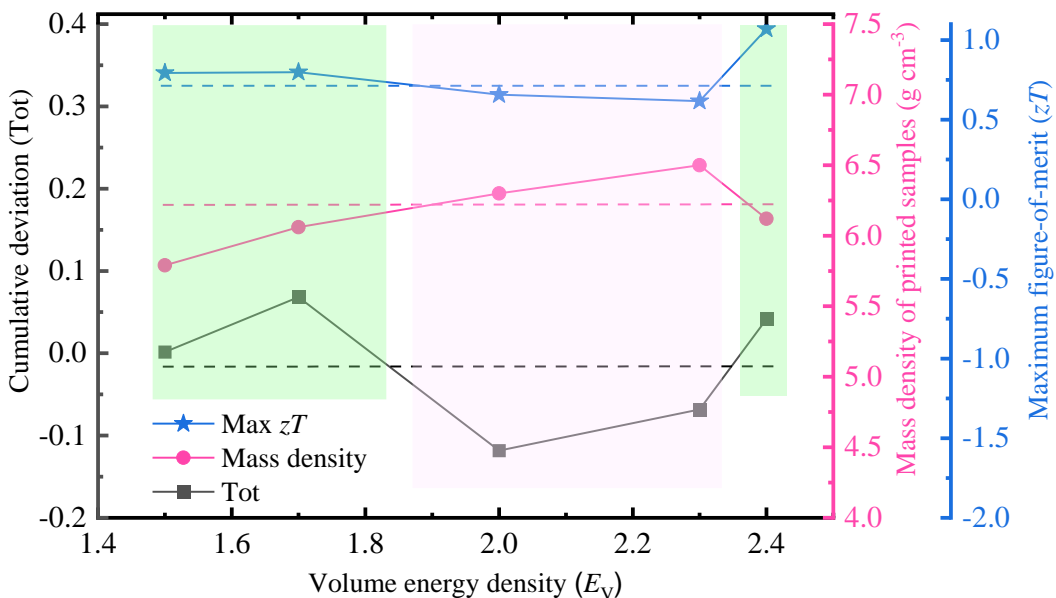
$$\text{Tot} = \vec{\lambda} \cdot (\vec{S} - \vec{S}_i) / \vec{S} \quad (2)$$

109 Where $\vec{\lambda}$ is a vector with three rows and one column and its value is [1; 1; 1], \vec{S} is the

110 vector of the designed atomic percent of elements Bi, Sb, and Te with stoichiometric
111 ratio $\text{Bi}_{0.5}\text{Sb}_{1.5}\text{Te}_3$ (BST), and its value is [10 20 30], \vec{S}_i ($i=1, 2, 3, 4, 5$) are vectors of
112 the tested atomic percent of composition elements Bi, Sb, and Te with printed samples.

113 The tested atomic percent is derived from **Table S3**. According to the calculation
114 of cumulative deviation, the resulting Tot is 0.0015, 0.0683, -0.1182, -0.0683, and
115 0.0415 corresponding to samples S1-1.5, S2-1.7, S3-2.0, S4-2.3 and S5-2.4 respectively.

116 It can be seen from **Fig. S8** that the Tot of composition element and maximum figure-
117 of-merit change with volume energy density very similarly. With the increase of E_v ,
118 Tot, and zT values are first reduced and then increased. However, the mass density of
119 printed samples, which is derived from **Table 1**, can first be added and then decreased
120 with the increase of volume energy density. When printing thermoelectric materials
121 BST at lower E_v (1.5 and 1.7 $\text{J}\cdot\text{mm}^{-3}$), all the powder material is not completely melted
122 and may exist inadequate chemical reactions due to excess tellurium, resulting in a
123 partial void and lower than the mass density of the zone-melted bulk. The E_v increases
124 to 2.0 and 2.3 $\text{J}\cdot\text{mm}^{-3}$, and the printing raw materials have undergone enough melting
125 to obtain dense bulk and complex chemical reactions to deviate designed atomic
126 percentage. The E_v is further increased to 2.4 $\text{J}\cdot\text{mm}^{-3}$, the elements with low heat of
127 evaporation, for instance, 114 kJ mol^{-1} for tellurium, 179 kJ mol^{-1} for bismuth and 193
128 kJ mol^{-1} for antimony, produce a certain degree of volatilization, resulting in certain
129 pores. Thereby, the resulted pores reduce the mass density, and the decrease in thermal
130 conductivity is derived from the reduction of mass density according to the relationship
131 $k=DC_p d$, where k is thermal conductivity, D is the thermal diffusivity, C_p is specific
132 heat capacity and d is the mass density. The thermoelectric performance is enhanced by
133 reducing thermal conductivity in the case of an unchanged power factor. So, the
134 relationship of processing-microstructure-property in printing-synthesizing BST is that
135 cumulative deviation of composition element increases first and then decreases with the
136 increase of E_v , and zT decreases as the deviation increases.



137
138 **Fig. S8.** The volume energy density dependence of cumulative deviation of
139 composition element in $\text{Bi}_{0.5}\text{Sb}_{1.5}\text{Te}_3$, mass density, and maximum figure-of-merit.

140 Reference

- 141 [1] T. DebRoy, T. Mukherjee, H. Wei, J. Elmer, J. Milewski, mechanistic models and
142 machine learning in metal printing, *Nature Reviews Materials* 6(1) (2021) 48-68.
143 [2] Y. Yan, H. Ke, J. Yang, C. Uher, X. Tang, Fabrication and Thermoelectric Properties
144 of n-Type $\text{CoSb}_{2.85}\text{Te}_{0.15}$ Using Selective Laser Melting, *ACS Applied Materials &*
145 *Interfaces* 10(16) (2018) 13669-13674.
146 [3] S. Kim, K. Lee, H. Mun, H. Kim, S. Hwang, J. Roh, D. Yang, W. Shin, X. Li, Y.
147 Lee, G. Snyder, S. Kim, Dense dislocation arrays embedded in grain boundaries
148 for high-performance bulk thermoelectrics, *Science* 348(6230) (2015) 109-114.
149 [4] Q. Zhang, R. Zhai, T. Fang, K. Xia, Y. Wu, F. Liu, X. Zhao, T. Zhu, Low-cost p-type
150 $\text{Bi}_{2}\text{Te}_{2.7}\text{Se}_{0.3}$ zone-melted thermoelectric materials for solid-state refrigeration,
151 *Journal of Alloys and Compounds* 831 (2020) 154732.
152 [5] J. Asai, M. Bumrungpon, T. Tsubochi, T. Kanaya, M. Tachii, T. Maeda, K. Hasezaki,
153 Shift of tellurium solid-solubility limit and enhanced thermoelectric performance
154 of bismuth antimony telluride milled with yttria-stabilized zirconia balls and
155 vessels, *Journal of the European Ceramic Society* 41(16) (2021) 188-194.
156 [6] Y. Zhang, Thermoelectric performance of graphene composited BiSbTe bulks by
157 high pressure synthesis, *Journal of Alloys and Compounds* 715 (2017) 344-348.
158 [7] M. Hong, Z. Chen, L. Yang, J. Zou, Enhancing thermoelectric performance of
159 Bi_2Te_3 -based nanostructures through rational structure design, *Nanoscale* 8(16)
160 (2016) 8681-8686.